

# Femtosecond x-ray photon correlation spectroscopy enables direct observations of atomic-scale relaxations of glass forming liquids

Cite as: J. Chem. Phys. 162, 194201 (2025); doi: 10.1063/5.0264574

Submitted: 11 February 2025 • Accepted: 22 April 2025 •

Published Online: 15 May 2025



View Online



Export Citation



CrossMark

Tomoki Fujita,<sup>1</sup> Yanwen Sun,<sup>2,a)</sup> Haoyuan Li,<sup>3</sup> Thies J. Albert,<sup>4</sup> Sanghoon Song,<sup>2</sup> Takahiro Sato,<sup>2</sup> Jens Moesgaard,<sup>1</sup> Antoine Cornet,<sup>5</sup> Peihao Sun,<sup>6</sup> Ying Chen,<sup>2</sup> Mianzhen Mo,<sup>2</sup> Narges Amini,<sup>1</sup> Fan Yang,<sup>7</sup> Pierre Lucas,<sup>8</sup> Vincent Esposito,<sup>2</sup> Joan Vila-Comamala,<sup>9</sup> Nan Wang,<sup>2</sup> Talgat Mamyrbayev,<sup>9</sup> Christian David,<sup>9</sup> Jerome Hastings,<sup>2</sup> Beatrice Ruta,<sup>5</sup> Paul Fuoss,<sup>2</sup> Klaus Sokolowski-Tinten,<sup>4</sup> Diling Zhu,<sup>2</sup> and Shuai Wei<sup>1,10,a)</sup>

## AFFILIATIONS

<sup>1</sup>Department of Chemistry, Aarhus University, 8000 Aarhus, Denmark

<sup>2</sup>Linac Coherent Light Source, SLAC National Accelerator Laboratory, Menlo Park, California 94025, USA

<sup>3</sup>Department of Mechanical Engineering, Stanford University, 440 Escondido Mall, Stanford, California 94305, USA

<sup>4</sup>Faculty of Physics and Center for Nanointegration Duisburg-Essen (CENIDE), University of Duisburg-Essen, Lotharstrasse 1, 47048 Duisburg, Germany

<sup>5</sup>Institut Néel, CNRS, 38042 Grenoble, France

<sup>6</sup>Department of Physics, Università degli Studi di Padova, 35122 Padova, Italy

<sup>7</sup>Institute of Materials Physics, Deutsches Zentrum für Luft- und Raumfahrt (DLR), Köln, Germany

<sup>8</sup>Department of Materials Science and Engineering, University of Arizona, Tucson, Arizona 85721, USA

<sup>9</sup>Paul Scherrer Institut, 5232 Villigen PSI, Switzerland

<sup>10</sup>Centre for Integrated Materials Research, Aarhus University, 8000 Aarhus, Denmark

<sup>a)</sup>Authors to whom correspondence should be addressed: [yanwen@slac.stanford.edu](mailto:yanwen@slac.stanford.edu) and [shuai.wei@chem.au.dk](mailto:shuai.wei@chem.au.dk)

## ABSTRACT

Glass-forming liquids exhibit structural relaxation behaviors, reflecting underlying atomic rearrangements on a wide range of timescales and playing a crucial role in determining material properties. However, the relaxation processes on the atomic scale are not well-understood due to the experimental difficulties in directly characterizing the evolving correlations of atomic-scale order in disordered systems. Here, we harness the coherence and ultrashort pulse characteristics of an x-ray free electron laser to directly probe atomic-scale ultrafast relaxation dynamics in the model system Ge<sub>15</sub>Te<sub>85</sub>. We demonstrate an analysis strategy for determining the intermediate scattering function by extracting the contrast decay of summed scattering patterns from two rapidly successive, nearly identical femtosecond x-ray pulses generated by a split-delay system. The result indicates a full decorrelation of atomic-scale order on the sub-picosecond timescale, supporting the argument for a high-fluidity fragile state of liquid Ge<sub>15</sub>Te<sub>85</sub> above its dynamic crossover temperature. The demonstrated strategy opens an avenue for experimental studies of relaxation dynamics in liquids, glasses, and other highly disordered systems.

Published under an exclusive license by AIP Publishing. <https://doi.org/10.1063/5.0264574>

## I. INTRODUCTION

Structural relaxation is a fundamental characteristic of all liquids and glasses, involving atomic rearrangements with time. The relaxation dynamics are extremely diverse, with the characteristic timescales ranging from millions of years for glass aging to some sub-picoseconds for fast relaxation processes in high-fluidity liquids. They are critical to many properties of glass forming systems, such as viscosity, vitrification, amorphous stability, and crystallization.<sup>1–5</sup> Relaxation dynamics are usually characterized by measuring time (or frequency)-dependent changes of macroscopic properties using techniques such as dynamic mechanical spectroscopy (DMS), dielectric spectroscopy, calorimetry, and rheology.<sup>4,6–9</sup> However, the atomic-level mechanisms of structural relaxations are often debated, as few experimental techniques can directly probe the atomic-scale structural relaxations in disordered systems. Over the past three decades, x-ray photon correlation spectroscopy (XPCS) based on synchrotron x-ray sources has been developed. By extracting intensity autocorrelation functions from measured speckle patterns,<sup>10–12</sup> the intermediate scattering function (ISF) can be determined, revealing the relaxation dynamics on atomic length scales.<sup>11</sup> However, XPCS has been limited to slow dynamics near and below the glass transition temperature  $T_g$ , and it has been challenging to make measurements on the microsecond timescale or below due to the limited coherent photon flux at synchrotron x-ray sources.<sup>13</sup>

Direct experimental access to faster relaxation dynamics is of particular interest because all liquids exhibit short relaxation times (i.e., high fluidity) at high temperatures, especially for those with a high liquid fragility. The fragility concept classifies the diverse variety of liquids according to their temperature dependence of relaxation times (or viscosity).<sup>14</sup> On approaching  $T_g$ , some liquids exhibit a near-Arrhenius rise in viscosity, classified as “strong,” while others, as “fragile liquids,” show a range of super-Arrhenius behavior.<sup>14</sup> While many liquids follow a simple fragile or strong behavior, some anomalous liquids exhibit a so-called fragile-to-strong transition (FST) (also referred as dynamic crossover).<sup>15–17</sup> A FST is usually accompanied by thermodynamic response function maxima (e.g., heat capacity and compressibility), as well as local structural changes.<sup>18–20</sup> Such a transition has been long debated in water<sup>15,21–23</sup> and suggested in silicon,<sup>24–27</sup> germanium,<sup>28</sup> oxides, molecular and metallic systems, and many others.<sup>16,17,29–31</sup> A clear FST has been demonstrated in liquid  $\text{Ge}_{15}\text{Te}_{85}$  near its eutectic melting point.<sup>18,32,33</sup> In the related systems (e.g.,  $\text{Ge}_{15}\text{Sb}_{85}$  and  $\text{AgInSbTe}$ ), the FST plays an important role in the functionality of phase-change memory devices.<sup>19,20,34</sup> Yet, understanding the atomic-level relaxation dynamics near these transitions presents a tremendous challenge because (1) FSTs reported in the literature typically occur far above  $T_g$  with a short relaxation timescale from nanoseconds to sub-picoseconds, far beyond the capability of synchrotron-based XPCS, and (2) FSTs are often hidden in the supercooled liquid below the melting temperature  $T_m$  obscured by fast crystallization.

X-ray free electron lasers (XFELs), delivering an unprecedentedly high number of photons within sub-100-femtosecond pulses that have nearly full transverse coherence, provide the opportunity to extend XPCS to probing dynamics in the ultrafast domain from femtosecond to nanosecond timescales. The key idea is that a femtosecond x-ray pulse is split into two nearly identical pulses with an

adjustable time delay in-between. As the double pulses scatter from the sample in rapid succession, the summed speckle patterns, collected by using a 2D detector, carry information about atomic-scale dynamics on the timescale of the double pulse separation. However, implementing this concept has faced technical challenges, including generating identical double pulses,<sup>35</sup> extremely low count rates (limited at wide angles due to the small scattering cross section from atomic scale order) of the order of  $10^{-4}$  photons/pixel,<sup>36</sup> and lack of robust analytical methods of separating real dynamics from noise or artifacts.

Pioneering studies have explored the feasibility of split-delay optics to deliver double x-ray pulses with identical properties,<sup>37–43</sup> required for extracting the intrinsic dynamics of the sample. The conventional division-of-wavefront split-delay systems, despite providing double pulses with good efficiency, suffer from the instability of the crystal-optics-based beam splitters and have difficulty in preserving sufficient mutual coherence between the two pulses.<sup>35</sup> A more recent approach, introduced by some of the authors of this work, employs transmission gratings as beam splitters and has successfully generated highly mutually coherent hard x-ray pulse pairs.<sup>44</sup> In addition, the femto- to pico-second separation of pulse pairs is beyond the time resolution of any x-ray detectors, which renders the data analysis strategy significantly different from that of synchrotron-based XPCS. Contrast extraction, relying on analyzing photon statistics of the summed speckles,<sup>36</sup> has been developed and utilized to obtain the ISF for nanoscale dynamics from measurements at small angles.<sup>45,46</sup> However, access to atomic-scale dynamics has been difficult due to the orders of magnitude lower scattering signals at wide angles. Concerns revolve around two key issues: (1) the double pulses might fail to maintain a high level of mutual stability during the extended period of data acquisition; (2) detector noise, artifacts, and background radiation may interfere with accurate extraction of speckle contrast. A recent study of water observed the speckle contrast decay with a split-delay system, possibly reflecting water's atomic-scale dynamics; yet, it is unclear whether the double-pulse overlap remained stable during the measurement and any drift in overlap would lead to errors in the measured dynamics.<sup>47</sup>

The glass forming system  $\text{Ge}_{15}\text{Te}_{85}$  is known to undergo a dynamic crossover above its eutectic melting point  $\sim 385$  °C, at around 400 °C, where the viscosity drops sharply by two orders of magnitude to a high-fluidity fragile state.<sup>18</sup> However, the atomic-level dynamics in this state have not been observed, making  $\text{Ge}_{15}\text{Te}_{85}$  an excellent initial system for developing and demonstrating the capabilities of XPCS at XFELs.

In this work, we probed the fragile state of  $\text{Ge}_{15}\text{Te}_{85}$  using the x-ray pulse pairs delivered by the aforementioned grating-based split-delay system.<sup>44</sup> Limited only by the x-ray pulse duration, this FEL-based XPCS methodology achieves femtosecond time resolution (fs-XPCS), enabling the study of atomic-scale dynamics in a wide range of disordered sample systems. We developed a protocol to account for the imperfect spatial overlap of the pulse pairs by simultaneously measuring the small-angle scattering (SAXS) and wide-angle scattering (WAXS) signals. We show that even with extremely low photon counts, contrast extraction by analyzing photon statistics allows for the observation of speckle contrast decay resulting from the sample dynamics. We demonstrate a strategy to determine the ISF on the sub-picosecond timescale, which provides

the direct atomic-level evidence of fast dynamics in  $\text{Ge}_{15}\text{Te}_{85}$  after it is transformed to a fragile liquid.

## II. RESULTS

### A. Experimental strategy for harnessing the coherence of double x-ray pulses in rapid succession

Figure 1 shows the schematic of the fs-XPCS experimental setup. The experiment was performed at the x-ray pump-probe instrument of the Linac Coherent Light Source (LCLS). The output pulse pairs from the split-delay system<sup>44</sup> have a photon energy of 9.5 keV and are focused on the sample location by a set of compound refractive beryllium lenses with a focal length of 1.5 m. The sample,  $\text{Ge}_{15}\text{Te}_{85}$ , is encapsulated in a quartz capillary with an inner diameter of about  $10\ \mu\text{m}$  and is resistively heated to the fragile liquid state at  $550\ ^\circ\text{C}$  (well above the eutectic melting point of  $385\ ^\circ\text{C}$ ). The sample temperature is constantly monitored by two thermocouples placed close to the sample position on both sides of the capillary. The temperature stability is within  $0.1\ ^\circ\text{C}$  throughout the measurements and the difference between two thermocouples stay within  $4\ ^\circ\text{C}$ . The focal spot size is  $\sim 2\ \mu\text{m}$  (FWHM), and the average pulse pair energy is characterized to be  $0.15\ \mu\text{J}$  at the sample plane. Four ePix100 detectors<sup>48</sup> are assembled in a  $2 \times 2$  array and placed  $2.5\ \text{m}$  downstream to cover the first structure factor  $S(Q)$  peak (at  $Q_0 = 2.0\ \text{\AA}^{-1}$ ) of the sample to probe its atomic-scale relaxation dynamics. The scattering signal-to-background ratio is optimized to be larger than 10. Another ePix100 detector is mounted  $5\ \text{m}$  downstream to simultaneously measure the SAXS signal, which originates mostly from the quartz capillary and allows for *in situ* characterization of the spatial overlap of the two pulses.

Ensuring the stable and highly overlapped condition of pulse pairs is essential for distinguishing intrinsic sample dynamics from many possible artifacts. In Fig. 1 (left panel), each XFEL pulse is split into two pulses via a diamond transmission grating.<sup>44</sup> The two pulses are directed by Bragg crystal reflections to travel along

different optical paths with the path length difference determining their time delay  $\Delta t$ . They are then recombined to the same trajectory by the other diamond grating further downstream. The pair of transmission gratings enables amplitude splitting to generate two collinear pulses, which is a prerequisite for performing ultrafast XPCS via speckle visibility analysis.<sup>35,44</sup> Transmissive intensity diagnostics consisting of a diode collecting the scattering signal from a Kapton target are placed in the optical paths of individual branches to measure their intensities on a shot-to-shot basis. One shot consists of a single pulse or a pulse pair, depending on the measurement mode. By installing shutters in the respective optical paths for the two beams, we can constantly cycle between three modes of pulses: (1) a single pulse per shot through the path length adjustable branch (i.e., delayed branch), (2) a single pulse per shot through the fixed path branch (i.e., fix-delay branch), and (3) a pulse pair per shot through both branches. As a result, speckle patterns for each shot were collected as “data frames” at both SAXS and WAXS detectors. Each data frame corresponds to one of the three modes (i.e., delayed, fix-delay, and both). By comparing the speckle contrast of SAXS signals from the three measurements, we are able to monitor the degree of transverse coherence as well as the spatial overlap of the two pulses continuously. This information provides feedback to the analysis of the wide-angle contrast degradation, mandatory for the accurate extraction of the ISF for studying sample dynamics, as discussed in the following.

The contrast of the summed speckle pattern from both beams ( $\beta_{\text{both}}$ ) can be related to that of the single branch beams ( $\beta_{\text{fix-delay}}$  and  $\beta_{\text{delayed}}$ ) with<sup>46</sup>

$$\beta_{\text{both}} = r^2 \beta_{\text{fix-delay}} + (1-r)^2 \beta_{\text{delayed}} + r(1-r)(\beta_{\text{fix-delay}} + \beta_{\text{delayed}})\mu F, \quad (1)$$

where  $F = |f|^2$  is the experimentally accessible quantity by fs-XPCS and  $f = f(Q, \Delta t)$  is the ISF to be determined for characterizing the relaxation dynamics, at a given scattering wavevector  $Q$  and a time delay  $\Delta t$ . The branching ratio  $r = i_{\text{fix-delay}} / (i_{\text{fix-delay}} + i_{\text{delayed}})$  is the

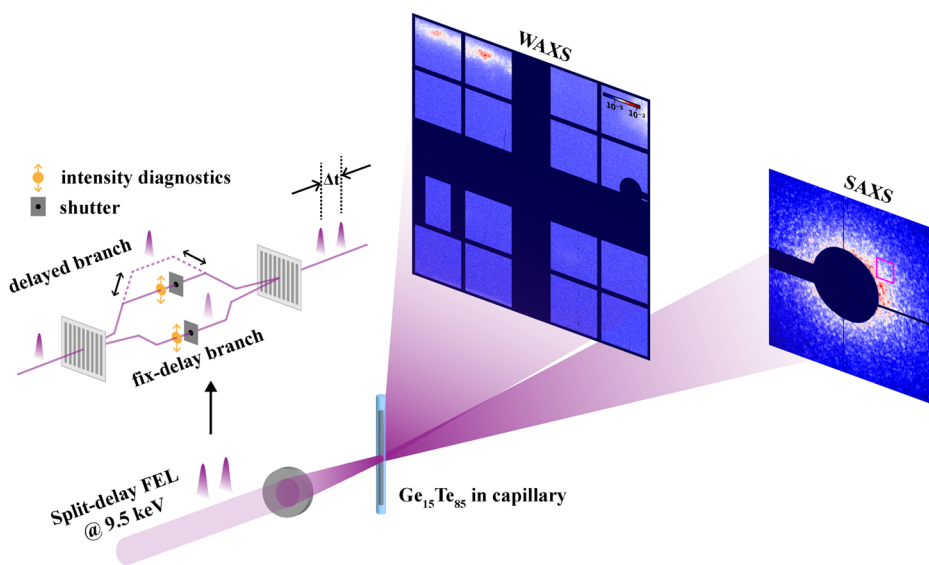


**FIG. 1.** Schematic of the experimental setup of the femtosecond x-ray photon correlation spectroscopy (fs-XPCS) experiment. The grating-based split-delay system is schematically shown on the left panel. An array of WAXS and SAXS detectors, placed downstream of the sample, collects speckle patterns at wide and small angles simultaneously. Here, we show the WAXS and SAXS patterns averaged over  $1 \times 10^6$  and 100 shots, respectively.

intensity fraction of the fix-delay branch in the pulse pair (see the [supplementary material](#), Sec. 1, for details regarding the intensity distribution of the split-delay system). The beam overlap coefficient  $\mu$  ( $0 \leq \mu \leq 1$ ) characterizes the effect due to the imperfect spatial overlap between the two branches.<sup>45</sup>  $\mu = 1$  corresponds to an ideal overlap, while in the case of  $\mu = 0$ , the two beams are probing different sample locations, and the contrast from their summed speckle pattern  $\beta_{\text{both}}$  no longer encodes sample dynamics, i.e., the ISF. We stress that since both  $\mu$  and the ISF contribute to the change in  $\beta_{\text{both}}$ , extracting the contrast changes alone does not yield the ISF. As a result, both a sufficiently high level of spatial overlap and a real-time diagnostic of the overlap coefficient are a prerequisite for accurately extracting the ISF. This diagnostic also enables live feedback during data collection. If  $\mu$  indicates a drift in the beam condition, we re-align the two pulses. This is accomplished by measuring the individual beam profiles on a scintillator-based profile monitor at the sample plane. Using the fix-delay beam as a reference, we adjust the position of the delayed beam via motion stacks of the crystal towers in the delayed branch.<sup>44</sup>

## B. Small-angle speckle contrast and spatial overlap of double pulses

As stated above, the SAXS intensity in the experiment, originating predominantly from quartz capillary, serves as a static reference,

i.e.,  $|f(Q, \Delta t)| = 1$ , as the observation timescale (of order  $\sim$ ps) is far smaller than the relaxation time of quartz glass (i.e., fused silica) in this low- $Q$  region at a temperature well below its  $T_g = 1173$  °C. We are, therefore, able to quantify  $\mu$  directly from the single and both beam SAXS contrasts. [Figures 2\(a\)–2\(c\)](#) show a region in the averaged speckle patterns of the SAXS data corresponding to the three measurement modes. Qualitatively, the high similarity of the three patterns already indicates an excellent spatial overlap between the two pulses. Their contrasts as a function of the measurement time are shown in the upper panel of [Fig. 2\(d\)](#). Since the transmissive intensity diagnostic provides a real-time measurement of the branching ratio, as shown in the middle panel, the overlap coefficient  $\mu$  can be derived using [Eq. \(1\)](#) and is shown in the lower panel. It is clear that  $\mu$  drifts on a minute timescale. The value of  $\mu$  remains mostly above 0.6, indicating a satisfactory overlap, thanks to the real-time monitoring and re-alignment of the beams, although  $\mu$  of some frames may occasionally drift below 0.6 [e.g., on Jun-05 9:30–10:00 as in [Fig. 2\(d\)](#)]. For the consistency of analysis, we have excluded the WAXS data frames with  $\mu < 0.6$ . Furthermore, an effective overlap value  $\bar{\mu}$  is derived from the averaged SAXS contrast values of the three modes during the exact same time span of the WAXS measurements. This value is then inserted into [Eq. \(1\)](#) to benchmark the WAXS contrast reduction and compute  $F$  for each time delay, as detailed in [Table I](#).

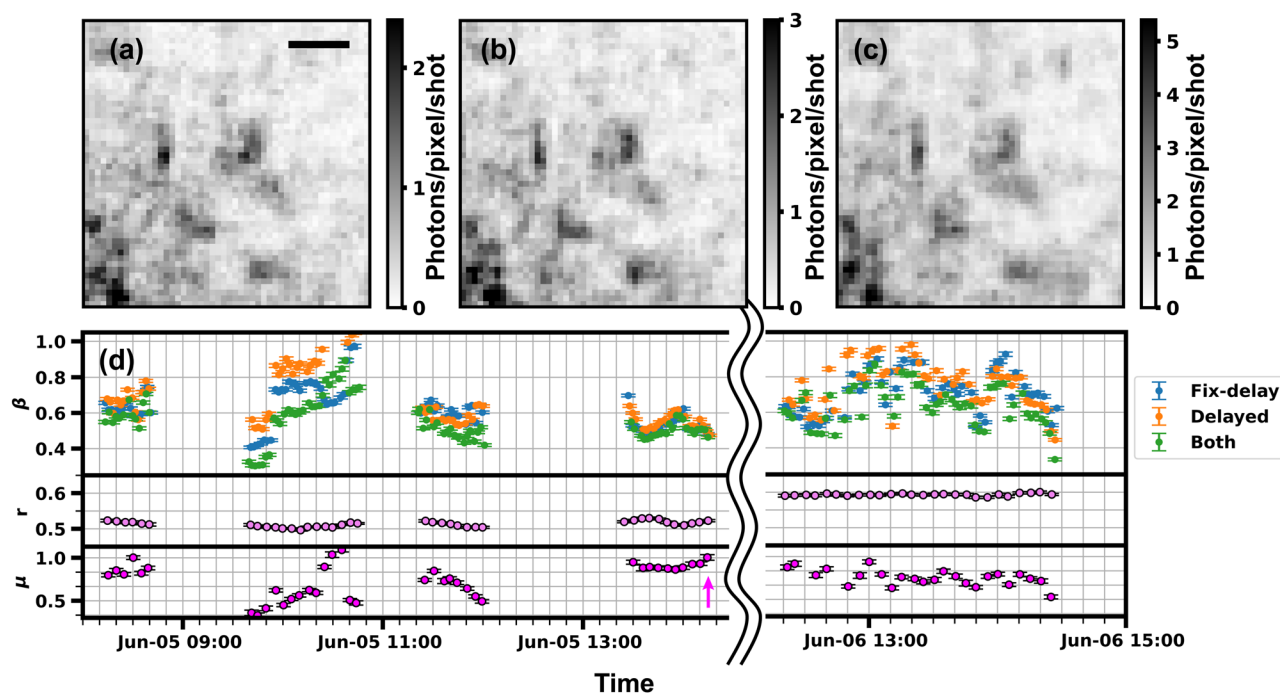


**FIG. 2.** Small-angle coherent scattering from the static reference for obtaining the real-time overlap coefficient of the pulse pairs. The speckle patterns are averaged over 40 frames for the delayed (a), fix-delay (b), and both (c) branch modes. They are measured, while collecting the wide-angle data, at the delay time of 0.1 ps. The displayed region corresponds to the square highlighted in magenta in the SAXS detector shown in [Fig. 1](#). The gray scales indicate the count rate and have a unit of photons/pixel/shot. The scale bar in panel (a) is the same for all three plots and corresponds to  $0.0005 \text{ \AA}^{-1}$ . (d) The speckle contrasts  $\beta$  (upper panel), the branching ratio  $r$  of the pulse pairs, and the overlap coefficient  $\mu$  (lower panel) obtained from the intensity diagnostic and the SAXS data with the elapse of the measurement time. During the same period, the wide-angle speckle data for 0.1 and 0.65 ps delays are collected, respectively. The magenta arrow points to the time when the speckles in panels (a)–(c) are measured.

**TABLE I.** Measurement statistics, parameters, and results including the count rate  $\bar{k}$ , the number of frames  $N_{\text{frame}}$  and pixels  $N_{\text{pixel}} \approx 7 \times 10^5$ , the speckle contrast levels  $\hat{\beta}$ , their error bars from both the maximum likelihood fitting  $\delta\beta_{\text{MLE}}$ , and the photon statistics  $\delta\beta_{\text{Poisson}}$  for the two delays, i.e., 0.1 and 0.65 ps. The effective overlap  $\bar{\mu}$  from the SAXS measurements and the averaged branching ratio  $\bar{r}$  from the intensity diagnostic, corresponding to the same period of WAXS data collection, are used to calculate  $F$ . The error, i.e., standard deviation, is reported in the parentheses.

$\Delta t$ (ps)	$\bar{k}$ (photons/pixel)	$N_{\text{frame}}$	$\hat{\beta}$	$\delta\beta_{\text{MLE}}$	$\delta\beta_{\text{Poisson}}$	$\bar{\mu}$	$\bar{r}$	$F$
0.1	$5.8 \times 10^{-5}$	257 250	0.17	0.05	0.05	0.80 (0.03)	0.51 (0.05)	1.3 (0.9)
0.65	$4.6 \times 10^{-5}$	283 067	0.04	0.05	0.05	0.76 (0.08)	0.59 (0.07)	-0.7 (0.8)

### C. Wide-angle speckle contrast and atomic-scale relaxation dynamics

The wide-angle speckle patterns collected at the first S(Q) maximum contain the information of the characteristic atomic-scale relaxation dynamics of the fragile liquid state. Since the scattering cross section from the atomic-scale order is limited, the count rate is on average about  $5 \times 10^{-5}$  photons/pixel per shot, with both beams illuminating the sample. It, therefore, requires a large number of data frames from detectors containing multi-million pixels and the careful treatment of artifacts including abnormal detector pixels, and background radiation from impurities in concrete and cosmic rays<sup>49</sup> to accurately extract the contrast values from photon statistics, i.e., from the probability of multiple photon per pixel events (see the [supplementary material](#), Sec. 2). The method of obtaining contrast from speckle patterns in the discrete photon limit has been demonstrated by Hruszkewycz *et al.* in Ref. 36, albeit at a much larger count rate, on average more than 0.01 photons/pixel. At this count rate, beam-induced permanent changes are visible when the sample was evaluated with a scanning electron microscope. It remains experimentally unclear whether the contrast extraction method can be further applied to even lower count rates in the non-perturbative regime, by simply extending the measurement time. Moreover, since monochromatic SASE (self-amplified spontaneous emission) pulses from an XFEL exhibit large intensity fluctuations,<sup>50</sup> it is essential to appropriately weigh the signal contribution of individual frames to the overall photon statistics. Therefore, we adopt a different approach to obtain the contrast by introducing a maximum likelihood-based contrast estimator (MLE). The likelihood ratio  $\chi^2$  is defined as<sup>45,51</sup>

$$\chi^2(\beta) = -2 \sum_{f=1}^{N_{\text{frame}}} \sum_{k=0}^{n_k} p_{f,k} N_{\text{pixel}} \ln \left( \frac{P_k(\beta, \bar{k}_f)}{p_{f,k}} \right). \quad (2)$$

For each frame  $f$  with available pixels  $N_{\text{pixel}}$ , the probabilities of each pixel having detected  $k = 0, 1, 2$  photons, denoted as  $p_{f,k}$ , are extracted from the WAXS data (we only consider up to  $n_k = 2$  photon/pixel events).  $p_{f,k}$  are then compared to the projected theoretical probability  $P_k$  [using Eq. (1) in the [supplementary material](#)] for a given count rate  $\bar{k}_f$ . The optimal estimate of the contrast,  $\hat{\beta}$ , is obtained by finding the minimum  $\chi^2$  values from the numerical calculations. The error  $\delta\beta_{\text{MLE}}$  can be retrieved by computing the second derivative of  $\chi^2$  at  $\hat{\beta}$ ,

$$\delta^2\beta_{\text{MLE}} = \left( \frac{\partial^2 \chi^2(\beta)}{2! \partial \beta^2} \right)^{-1} \Big|_{\beta=\hat{\beta}}. \quad (3)$$

This method is used to determine the contrast values for each mode of WAXS measurements, including the two single-pulse modes (i.e., fix-delay and delayed branch) as well as the both-beam mode at 0.1 and 0.65 ps, as shown in Fig. 3 of the [supplementary material](#). We furthermore plot the results of the contrast extraction, which converges with an increasing number of frames [see Figs. 3(a) and 3(b)]. The error bars are estimated using Eq. (3). For the two delays, i.e., 0.1 and 0.65 ps, the difference in their contrast becomes significantly larger than their errors when accumulating over 100 000 shots. Adding more frames further reduces the error, with the final values summarized in Table I. Strikingly, the MLE error  $\delta\beta_{\text{MLE}}$  is in an excellent agreement with the error derived from the photon counting statistics,

$$\delta\beta_{\text{Poisson}} = \frac{1}{\bar{k}} \sqrt{\frac{2(1 + \hat{\beta})}{(1 + M)N_{\text{pixel}}N_{\text{frame}}}}, \quad (4)$$

where  $M \approx 1$  characterizes the intensity fluctuations of the double pulses incident onto the sample (see the [supplementary material](#) Sec. 2 for the derivation). Such a high level of agreement shows that Eq. (2) is an efficient contrast estimator, and the shot noise is the main source of error even at this extremely low count rate. This agreement is non-trivial because it suggests that the measurement accuracy of the fs-XPCS experiment is merely limited by photon statistics and thus can be only improved by increasing data volume. It is also worth noting that due to the count rate being halved, the error bars for the single-pulse contrasts are larger compared to those in the both-beam mode despite that they are calculated using more than half a million frames, as shown in Fig. 3(a).

With the wide-angle contrasts in the single-pulse and both-beam mode, the effective overlap coefficient  $\bar{\mu}$  from the SAXS monitor, and the averaged branching ratio  $\bar{r}$  from the intensity diagnostics,  $F$ , for each delay can be determined using Eq. (1). In particular,  $F = 1.3 \pm 0.9$  for 0.1 ps and  $F = -0.7 \pm 0.8$  for 0.65 ps are obtained (Table I) and denoted as  $F(0.1 \text{ ps})$  and  $F(0.65 \text{ ps})$ , respectively. Due to the shot noises, relatively large error bars are present for both  $F$  values. To determine the presence of a decorrelation, the statistical significance of the difference between the two  $F$  values must be evaluated. Therefore, we performed a Monte Carlo statistics analysis for the two delay points. In this analysis, we assumed two normal distributions of possible values of  $F$  at the two delay

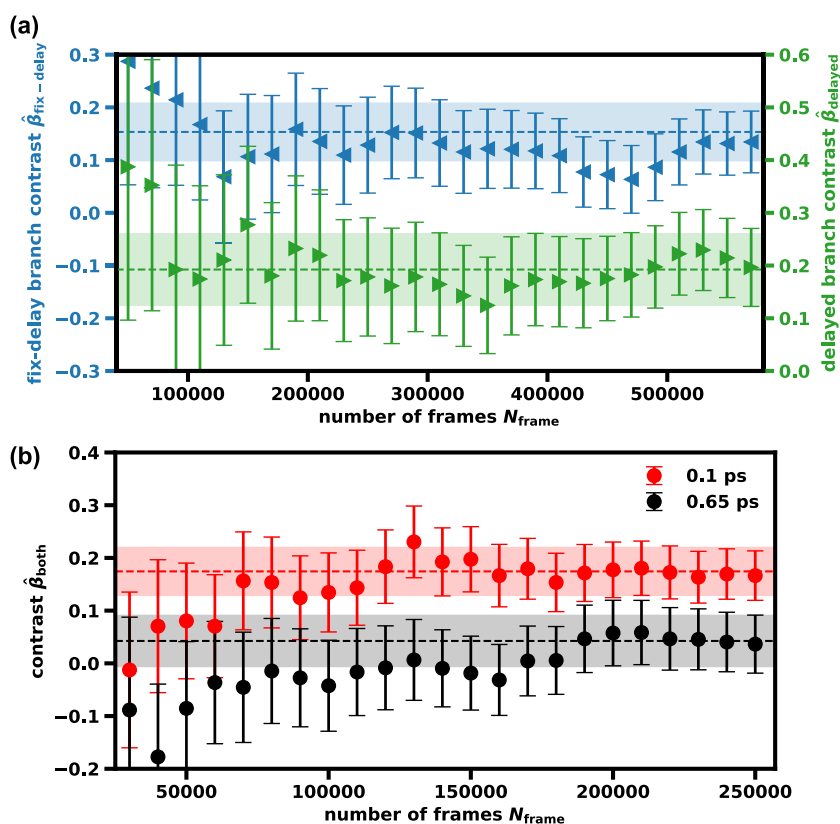


**FIG. 3.** Convergence of contrasts for (a) single-pulse and (b) both-beam mode. For each beam condition, the dashed line and the shaded area show the final contrast value and the MLE error when using all the data, respectively, which correspond to the [supplementary material](#), Fig. 3. The contrasts for the fix-delay (blue) and the delayed branch (green) in panel (a) are offset by using double y axes for clarity. For the both-beam mode in panel (b), the clear difference in the final contrast values between 0.1 and 0.65 ps indicates contrast decay.

points and generated a sufficiently large number (i.e., 10 000 000) of random numbers for the two distributions, with the mean values corresponding to the  $F(0.1 \text{ ps})$  and  $F(0.65 \text{ ps})$ , respectively, and the standard deviations representing the errors. We then performed a simulation by sampling these numbers and compared each value against  $1/e$ , as well as compared the values drawn from each of the distributions. This procedure then gives the probabilities of the three conditions: (1) the probability for  $F(0.1 \text{ ps}) > 1/e$  is 85%; (2) the probability for  $F(0.65 \text{ ps}) < 1/e$  is 91%; and (3) the probability for  $F(0.65 \text{ ps}) < F(0.1 \text{ ps})$  is 95%. These results indicate that our measurement has successfully captured the drop in ISF between the two delay points (with 95% confidence level). Since the timescale of decorrelation corresponds to the time when  $F$  decays to, typically,  $1/e$ , the value of  $F(0.1 \text{ ps})$  suggests that the sample retains substantial correlation, whereas  $F(0.65 \text{ ps})$  reflects almost full decorrelation. This suggests that the characteristic relaxation time  $\tau$  at  $550^\circ\text{C}$  is most likely within the range of 0.1–0.65 ps. This resulting  $\tau$  range is well consistent with the  $\tau_s \approx 0.29 \text{ ps}$  inferred from the Adam–Gibbs equation (see the [supplementary material](#), Sec. 4), as expected from the highly fragile behavior of  $\text{Ge}_{15}\text{Te}_{85}$  above its FST temperature.<sup>18</sup> To this end, we have successfully extracted atomic-level sub-picosecond dynamics of a high fluidity liquid state from the fs-XPCS experiment. An important consideration in XPCS measurements is the potential beam-induced effects. By directly examining contrast degradation at varying incident flux levels, we have shown that the contrast values remain consistent within the error margin,

when varying pulse influx, and thus ruled out the possibility of first pulse induced dynamics (see the [supplementary material](#), Sec. 3).

### III. DISCUSSION

Our results demonstrate the strategy for XFEL-based XPCS, attaining femtosecond temporal and atomic-scale spatial resolution. This extends the lower boundary of the accessible timescale by 12 orders of magnitude from the millisecond regime of synchrotron-based XPCS.<sup>52</sup> The latter has been a major experimental tool in the past decade for understanding the atomic-level relaxation dynamics near or below  $T_g$  in glasses.<sup>4,10,53,54</sup> By adjusting the optical path of the delayed branch, the split-delay system enables probing the timescales from femto- to several nanoseconds.<sup>37–42</sup> Individual pulses separated by tens to hundreds of nanoseconds can be produced by the nanosecond double-bunch mode using accelerator techniques,<sup>55</sup> as demonstrated in a study of colloidal dynamics.<sup>46</sup> At the European XFEL, the unique time structure of intra-train MHz pulses is shown to enable XPCS to cover the timescale of  $\sim\mu\text{s}$ .<sup>56</sup> Corresponding to the wide range of timescales, the entire temperature range of the Angell plot<sup>14</sup> is thus covered from the ultraviscous strong liquid near  $T_g$  to the highly fragile liquid well above its melting point. Unlike the frequency-domain analysis performed in inelastic scattering experiments, direct measurements in the time-domain with XPCS also give access to higher order time correlations.<sup>11</sup> This information is intrinsic to, and revealing

of, temporally heterogeneous dynamics in disordered systems.<sup>57,58</sup> Recent work by Böhmer *et al.*,<sup>59</sup> using multispeckle dynamic light-scattering measurements, demonstrated an experimental determination of “material time” (a concept coined to describe the intrinsic time measured on a clock whose rate changes with glass aging) in glass formers near  $T_g$ . The authors stressed that time-domain experiments are preferred to access material time,<sup>59</sup> as it can, in principle, access instantaneous autocorrelations even when aging or decorrelation takes place on comparable timescales that may change material properties. Thus, XFEL-based XPCS promises to be a crucial technique to determine material time in fast aging systems well above  $T_g$  (e.g., an undercooled liquid just below the melting point).

In these contexts, the XFEL-based fs-XPCS using separated pulse pairs may open a new avenue for studying the atomic-scale structural relaxations in uncharted territories (obscured by extremely fast relaxation or other fast competing processes such as crystallization) in the glass and liquid sciences. For instance, one could implement a laser-pulse pump shortly before the double x-ray pulses and probe the dynamics during the rapid melt-and-quench process of a liquid before fast crystallization interferes. This necessitates a high cooling rate, achievable only with the small sample sizes, as permitted by x-ray scattering. Such a pump-and-double-probe scheme might be used to access the relaxation dynamics of supercooled water below its homogeneous nucleation limit of 231 K<sup>60</sup> (termed as “no-man’s land”), where the origin of the well-known thermodynamic anomalies has been debated for decades.<sup>61</sup> Poor glass forming phase-change materials (e.g., Ge<sub>15</sub>Sb<sub>85</sub> and others<sup>19,20</sup>) undergo a metal-to-semiconductor fragile–strong transition during supercooling (20%–30% below  $T_m$ ) before they crystallize within a few nanoseconds. Measuring the atomic-scale relaxation dynamics near these “short-lived” transitions is of particular relevance for understanding the functionality of these materials in phase-change memory devices.

Although inelastic (and quasi-elastic) neutron scattering is conventionally used to measure dynamics on the energy transfer of meV to  $\mu$ eV, corresponding to timescales from picoseconds to nanoseconds, these techniques require a large sample and beam size, on the order of one to several centimeter, due to the weak interaction of neutrons with matter and the limited neutron flux. This makes it difficult to achieve substantial undercooling in liquids that are poor glass formers, or produce a large quantity of samples. In addition, neutron incoherent scattering occurs usually in the meV energy transfer range, interfering the signal of interest for coherent atomic dynamics.<sup>62</sup> As an alternative frequency-domain technique, inelastic x-ray scattering (IXS) can probe small samples with a focused x-ray beam ( $\sim 10$ – $100 \mu\text{m}$  beam spot size).<sup>62</sup> Owing to the high energy of x-rays of order  $\sim 10$  keV, the energy resolution of IXS is limited and is thus suited to probe large energy transfer of scattering (e.g., phonon dynamics). Yet, resolving meV energy transfer requires extremely high energy resolution  $\Delta E/E \sim 10^{-7}$ .<sup>62</sup> Recent progress of high-resolution IXS makes it possible to probe 1–100 meV; however, resolving  $\sim 1$  meV or below (i.e., order of  $\sim 1$  ps or larger) remains increasingly challenging.<sup>62</sup>

It is worth noting that  $\sim 1.7 \times 10^6$  frames are analyzed in this study to determine the ISF at two delay points. The number of delay points is constrained by the data collection rate, which is mainly limited by the pulse repetition rate of 120 Hz presently available at the LCLS, and the precision of our measurements is primarily limited

by shot noise. Thus, data collection for each delay point requires several hours. However, this scenario will undergo a transformative change with the advent of the LCLS-II-HE, which will provide hard x-ray pulses with MHz repetition rates.<sup>63</sup> Together with cutting-edge multi-mega-pixel x-ray detectors such as CITIUS,<sup>64</sup> SParkPix-S,<sup>65</sup> and AGIPD,<sup>66</sup> which operate at tens of kHz to MHz frame rates, it naturally allows us to collect data at substantially higher rates ( $\sim$ four orders of magnitude faster), potentially reducing the measurement time per delay point to tens of seconds. The methodology demonstrated in this work can then be efficiently employed to investigate the structural relaxation over the entire temperature range where the dynamic crossovers may occur. We note that since potential beam-induced effects could depend on specific systems, deposited energy, and repetition rates, systematic investigation is worth pursuing in future studies across diverse systems. Finally, the picosecond timescale of relaxation dynamics is readily accessible through standard computer simulations. The approach here, therefore, holds potential for bridging the gap between experimental observations and molecular dynamics simulations.

## SUPPLEMENTARY MATERIAL

The [supplementary material](#) provides (1) intensity distribution of the double pulses from the split-delay system; (2) contrast extraction and calibration; (3) evaluation of the x-ray beam perturbation; and (4) the prediction curve based on the Adam–Gibbs equation. Figures 1–5 ([supplementary material](#)).

## ACKNOWLEDGMENTS

Y.S. thanks Mark Sutton from experimental design to data analysis for many inspiring discussions. S.W. and Y.S. thank Peter Zalden for his helpful comments on the manuscript. Use of the Linac Coherent Light Source (LCLS), SLAC National Accelerator Laboratory, is supported by the U.S. Department of Energy, Office of Science, Office of Basic Energy Sciences under Contract No. DE-AC02-76SF00515. This work was supported by a research grant (No. 42116) from VILLUM FONDEN (S.W., T.F.) and partially supported by Deutsche Forschungsgemeinschaft (DFG, German Research Foundation) (No. WE 6440/1-1). B.R. and A.C. acknowledge funding for this project from the European Research Council (ERC) under the European Union’s Horizon 2020 research and innovation programme (Grant Agreement No. 948780). We acknowledge the Danish Agency for Science, Technology, and Innovation for funding the instrument center DanScatt and ESS SMART Lighthouse. K.S.-T. and T.J.A. acknowledge financial support from the DFG through Project No. 278162697-SFB 1242. P.L. acknowledges financial support from NSF-DMR under Grant No. 1832817. Work of H.L. was supported by U.S. Department of Energy, Office of Science under DOE (BES) Award No. DE-SC0022222.

## AUTHOR DECLARATIONS

### Conflict of Interest

The authors have no conflicts to disclose.

## Author Contributions

**Tomoki Fujita:** Formal analysis (lead); Investigation (equal); Methodology (equal); Visualization (equal); Writing – original draft (equal); Writing – review & editing (equal). **Yanwen Sun:** Conceptualization (equal); Data curation (equal); Formal analysis (equal); Investigation (equal); Methodology (equal); Software (equal); Visualization (equal); Writing – original draft (equal); Writing – review & editing (equal). **Haoyuan Li:** Data curation (equal); Investigation (supporting); Methodology (supporting). **Thies J. Albert:** Formal analysis (supporting); Investigation (supporting); Writing – review & editing (supporting). **Sanghoon Song:** Data curation (equal); Investigation (supporting); Methodology (supporting). **Takahiro Sato:** Data curation (supporting). **Jens Moesgaard:** Investigation (supporting); Methodology (supporting). **Antoine Cornet:** Investigation (supporting); Methodology (supporting). **Peihao Sun:** Formal analysis (supporting). **Ying Chen:** Investigation (supporting). **Mianzhen Mo:** Data curation (supporting); Investigation (supporting); Writing – review & editing (supporting). **Narges Amini:** Investigation (supporting). **Fan Yang:** Formal analysis (supporting); Investigation (supporting); Writing – review & editing (supporting). **Pierre Lucas:** Investigation (supporting); Methodology (supporting). **Vincent Esposito:** Software (equal). **Joan Vila-Comamala:** Investigation (supporting). **Nan Wang:** Investigation (supporting). **Talgat Mamyrbayev:** Investigation (supporting). **Christian David:** Investigation (supporting). **Jerome Hastings:** Investigation (supporting). **Beatrice Ruta:** Investigation (supporting); Methodology (supporting); Writing – review & editing (supporting). **Paul Fuoss:** Investigation (supporting); Methodology (supporting); Writing – review & editing (supporting). **Klaus Sokolowski-Tinten:** Investigation (supporting); Methodology (supporting); Writing – review & editing (supporting). **Diling Zhu:** Data curation (supporting); Investigation (supporting); Methodology (supporting); Writing – review & editing (supporting). **Shuai Wei:** Conceptualization (equal); Formal analysis (equal); Funding acquisition (equal); Investigation (equal); Methodology (equal); Project administration (equal); Supervision (equal); Writing – original draft (equal); Writing – review & editing (equal).

## DATA AVAILABILITY

The data that support the findings of this study are available from the corresponding authors upon reasonable request.

## REFERENCES

- W. H. Wang, “Dynamic relaxations and relaxation-property relationships in metallic glasses,” *Prog. Mater. Sci.* **106**, 100561 (2019).
- C. A. Angell, K. L. Ngai, G. B. McKenna, P. F. McMillan, and S. W. Martin, “Relaxation in glassforming liquids and amorphous solids,” *J. Appl. Phys.* **88**, 3113 (2000).
- H. Tanaka, “Roles of liquid structural ordering in glass transition, crystallization, and water’s anomalies,” *J. Non-Cryst. Solids: X* **13**, 100076 (2022).
- B. Ruta, E. Pineda, and Z. Evenson, “Relaxation processes and physical aging in metallic glasses,” *J. Phys.: Condens. Matter* **29**, 503002 (2017).
- J. C. Dyre, “Colloquium: The glass transition and elastic models of glass-forming liquids,” *Rev. Mod. Phys.* **78**, 953 (2006).
- X. Monnier, D. Cangialosi, B. Ruta, R. Busch, and I. Gallino, “Vitrification decoupling from  $\alpha$ -relaxation in a metallic glass,” *Sci. Adv.* **6**, eaay1454 (2020).
- Y. Cheng *et al.*, “Highly tunable  $\beta$ -relaxation enables the tailoring of crystallization in phase-change materials,” *Nat. Commun.* **13**, 7352 (2022).
- E. R. Weeks, J. C. Crocker, A. C. Levitt, A. Schofield, and D. A. Weitz, “Three-dimensional direct imaging of structural relaxation near the colloidal glass transition,” *Science* **287**, 627 (2000).
- R. Richert, “Supercooled liquids and glasses by dielectric relaxation spectroscopy,” *Adv. Chem. Phys.* **156**, 101 (2014).
- B. Ruta *et al.*, “Atomic-scale relaxation dynamics and aging in a metallic glass probed by x-ray photon correlation spectroscopy,” *Phys. Rev. Lett.* **109**, 165701 (2012).
- O. G. Shpyrko, “X-ray photon correlation spectroscopy,” *J. Synchrotron Radiat.* **21**, 1057 (2014).
- B. Ruta *et al.*, “Wave-vector dependence of the dynamics in supercooled metallic liquids,” *Phys. Rev. Lett.* **125**, 055701 (2020).
- G. Grübel, G. Stephenson, C. Gutt, H. Sinn, and T. Tschentscher, “XPCS at the European X-ray free electron laser facility,” *Nucl. Instrum. Methods Phys. Res., Sect. B* **262**, 357 (2007).
- C. A. Angell, “Formation of glasses from liquids and biopolymers,” *Science* **267**, 1924 (1995).
- C. A. Angell, “Liquid fragility and the glass transition in water and aqueous solutions,” *Chem. Rev.* **102**, 2627 (2002).
- H. Tanaka, “Liquid-liquid transition and polyamorphism,” *J. Chem. Phys.* **153** (2020).
- S. Wei, “Anomalous liquids on a new landscape: From water to phase-change materials,” *J. Non-Cryst. Solids: X* **14**, 100094 (2022).
- S. Wei, P. Lucas, and C. A. Angell, “Phase change alloy viscosities down to  $T_g$  using adam-gibbs-equation fittings to excess entropy data: A fragile-to-strong transition,” *J. Appl. Phys.* **118**, 034903 (2015).
- P. Zalden *et al.*, “Femtosecond x-ray diffraction reveals a liquid-liquid phase transition in phase-change materials,” *Science* **364**, 1062 (2019).
- S. Wei, P. Lucas, and C. A. Angell, “Phase-change materials: The view from the liquid phase and the metallicity parameter,” *MRS Bull.* **44**, 691 (2019).
- P. Gallo *et al.*, “Water: A tale of two liquids,” *Chem. Rev.* **116**, 7463 (2016).
- K. H. Kim *et al.*, “Maxima in the thermodynamic response and correlation functions of deeply supercooled water,” *Science* **358**, 1589 (2017).
- A. Dehaoui, B. Isenmann, and F. Caupin, “Viscosity of deeply supercooled water and its coupling to molecular diffusion,” *Proc. Natl. Acad. Sci. U. S. A.* **112**, 12020 (2015).
- S. Sastry and C. Austen Angell, “Liquid-liquid phase transition in supercooled silicon,” *Nat. Mater.* **2**, 739 (2003).
- N. Jakse and A. Pasturel, “Liquid-liquid phase transformation in silicon: Evidence from first-principles molecular dynamics simulations,” *Phys. Rev. Lett.* **99**, 205702 (2007).
- G. Zhao *et al.*, “Phase behavior of metastable liquid silicon at negative pressure: *Ab initio* molecular dynamics,” *Phys. Rev. B* **93**, 140203 (2016).
- V. V. Vasisht, S. Saw, and S. Sastry, “Liquid-liquid critical point in supercooled silicon,” *Nat. Phys.* **7**, 549 (2011).
- M. H. Bhat *et al.*, “Vitrification of a monatomic metallic liquid,” *Nature* **448**, 787 (2007).
- L. Henry *et al.*, “Liquid-liquid transition and critical point in sulfur,” *Nature* **584**, 382 (2020).
- L. Xu, I. Ehrenberg, S. V. Buldyrev, and H. E. Stanley, “Relationship between the liquid-liquid phase transition and dynamic behaviour in the Jagla model,” *J. Phys.: Condens. Matter* **18**, S2239 (2006).
- M. Stolpe *et al.*, “Structural changes during a liquid-liquid transition in the deeply undercooled  $Zr_{58.5}Cu_{15.6}Ni_{12.8}Al_{10.3}Nb_{2.8}$  bulk metallic glass forming melt,” *Phys. Rev. B* **93**, 014201 (2016).
- J. Pries, S. Wei, F. Hoff, P. Lucas, and M. Wuttig, “Control of effective cooling rate upon magnetron sputter deposition of glassy  $Ge_{15}Te_{85}$ ,” *Scr. Mater.* **178**, 223 (2020).
- H. Weber, J. Orava, I. Kaban, J. Pries, and A. L. Greer, “Correlating ultrafast calorimetry, viscosity, and structural measurements in liquid  $GeTe$  and  $Ge_{15}Te_{85}$ ,” *Phys. Rev. Mater.* **2**, 093405 (2018).

- <sup>34</sup>J. Orava, D. W. Hewak, and A. L. Greer, "Fragile-to-strong crossover in supercooled liquid Ag-In-Sb-Te studied by ultrafast calorimetry," *Adv. Funct. Mater.* **25**, 4851 (2015).
- <sup>35</sup>Y. Sun *et al.*, "Realizing split-pulse x-ray photon correlation spectroscopy to measure ultrafast dynamics in complex matter," *Phys. Rev. Res.* **2**, 023099 (2020).
- <sup>36</sup>S. O. Hruszkewycz *et al.*, "High contrast x-ray speckle from atomic-scale order in liquids and glasses," *Phys. Rev. Lett.* **109**, 185502 (2012).
- <sup>37</sup>W. Roseker *et al.*, "Performance of a picosecond x-ray delay line unit at 839 keV," *Opt. Lett.* **34**, 1768 (2009).
- <sup>38</sup>T. Osaka *et al.*, "A Bragg beam splitter for hard x-ray free-electron lasers," *Opt. Express* **21**, 2823 (2013).
- <sup>39</sup>T. Osaka *et al.*, "Wavelength-tunable split-and-delay optical system for hard x-ray free-electron lasers," *Opt. Express* **24**, 9187 (2016).
- <sup>40</sup>D. Zhu *et al.*, "Development of a hard x-ray split-delay system at the linac coherent light source," *Proc. SPIE* **10237**, 102370R (2017).
- <sup>41</sup>W. Lu *et al.*, "Development of a hard X-ray split-and-delay line and performance simulations for two-color pump-probe experiments at the European XFEL," *Rev. Sci. Instrum.* **89**, 063121 (2018).
- <sup>42</sup>R. Rysov, W. Roseker, M. Walther, and G. Grübel, "Compact hard X-ray split-and-delay line for studying ultrafast dynamics at free-electron laser sources," *J. Synchrotron Radiat.* **26**, 1052 (2019).
- <sup>43</sup>Y. Sun *et al.*, "Compact hard x-ray split-delay system based on variable-gap channel-cut crystals," *Opt. Lett.* **44**, 2582 (2019).
- <sup>44</sup>H. Li *et al.*, "Generation of highly mutually coherent hard-x-ray pulse pairs with an amplitude-splitting delay line," *Phys. Rev. Res.* **3**, 043050 (2021).
- <sup>45</sup>W. Roseker *et al.*, "Towards ultrafast dynamics with split-pulse X-ray photon correlation spectroscopy at free electron laser sources," *Nat. Commun.* **9**, 1704 (2018).
- <sup>46</sup>Y. Sun *et al.*, "Nonuniform flow dynamics probed by nanosecond x-ray speckle visibility spectroscopy," *Phys. Rev. Lett.* **127**, 058001 (2021).
- <sup>47</sup>Y. Shinohara *et al.*, "Split-pulse x-ray photon correlation spectroscopy with seeded x-rays from x-ray laser to study atomic-level dynamics," *Nat. Commun.* **11**, 6213 (2020).
- <sup>48</sup>M. Sikorski *et al.*, "Application of an ePix100 detector for coherent scattering using a hard x-ray free-electron laser," *J. Synchrotron Radiat.* **23**, 1171 (2016).
- <sup>49</sup>A. Q. R. Baron and D. Ishikawa, "Background rates in several hard x-ray photon counting pixel array detectors," *Nucl. Instrum. Methods Phys. Res., Sect. A* **1049**, 168101 (2023).
- <sup>50</sup>D. Zhu *et al.*, "Performance of a beam-multiplexing diamond crystal monochromator at the linac coherent light source," *Rev. Sci. Instrum.* **85** (2014).
- <sup>51</sup>S. S. Wilks, "The large-sample distribution of the likelihood ratio for testing composite hypotheses," *Ann. Math. Stat.* **9**, 60 (1938).
- <sup>52</sup>E. Alfinelli *et al.*, "Amorphous-amorphous transformation induced in glasses by intense x-ray beams," *Phys. Rev. B* **107**, 054202 (2023).
- <sup>53</sup>V. Di Lisio *et al.*, "Size-dependent vitrification in metallic glasses," *Nat. Commun.* **14**, 4698 (2023).
- <sup>54</sup>Z.-Y. Zhou, Q. Yang, and H.-B. Yu, "Toward atomic-scale understanding of structure-dynamics-properties relations for metallic glasses," *Prog. Mater. Sci.* **145**, 101311 (2024).
- <sup>55</sup>F. Decker *et al.*, "Two bunches with ns-separation with LCLS," in *Proceedings of FEL2015 WEP023* (JACoW Publishing, 2015), p. 634.
- <sup>56</sup>A. Madsen *et al.*, "Materials imaging and dynamics (MID) instrument at the european x-ray free-electron laser facility," *J. Synchrotron Radiat.* **28**, 637 (2021).
- <sup>57</sup>A. Madsen, R. L. Leheny, H. Guo, M. Sprung, and O. Czakkel, "Beyond simple exponential correlation functions and equilibrium dynamics in x-ray photon correlation spectroscopy," *New J. Phys.* **12**, 055001 (2010).
- <sup>58</sup>Z. Evenson *et al.*, "X-ray photon correlation spectroscopy reveals intermittent aging dynamics in a metallic glass," *Phys. Rev. Lett.* **115**, 175701 (2015).
- <sup>59</sup>T. Böhmer *et al.*, "Time reversibility during the ageing of materials," *Nat. Phys.* **20**, 637 (2024).
- <sup>60</sup>H. Kanno and C. A. Angell, "Water: Anomalous compressibilities to 1.9 kbar and correlation with supercooling limits," *J. Chem. Phys.* **70**, 4008–4016 (1979).
- <sup>61</sup>K. H. Kim *et al.*, "Experimental observation of the liquid-liquid transition in bulk supercooled water under pressure," *Science* **370**, 978–982 (2020).
- <sup>62</sup>A. Q. Baron, in *Synchrotron Light Sources and Free-Electron Lasers: Accelerator Physics, Instrumentation and Science Applications*, edited by E. J. Jaeschke, S. Khan, J. R. Schneider, and J. B. Hastings (Springer, 2020), pp. 2131–2212.
- <sup>63</sup>T. Raubenheimer *et al.*, "The LCLS-II-HE, a high energy upgrade of the LCLS-II," in *60th ICFA Advanced Beam Dynamics Workshop on Future Light Sources MOP1WA02* (JACoW Publishing, 2018), p. 6.
- <sup>64</sup>H. Nishino *et al.*, "The false beat signal of a high-speed x-ray imaging detector for synchrotron radiation experiments and its elimination with a synchronized CITIUS detector," *Nucl. Instrum. Methods Phys. Res., Sect. A* **1057**, 168710 (2023).
- <sup>65</sup>L. Rota, "SparkPix-ED: A readout ASIC with 1 MHz frame-rate for rare event experiments at LCLS-II," in *24th International Workshops on Radiation Imaging Detectors* (2023).
- <sup>66</sup>A. Allahgholi *et al.*, "The adaptive gain integrating pixel detector at the European XFEL," *J. Synchrotron Radiat.* **26**, 74 (2019).